Symmorphic intersecting nodal rings in semiconducting layers

Cheng Gong[1], Yuee Xie[1], Yuanping Chen[1]*, Heung-sik Kim[2] and David Vanderbilt[2]

[1]*School of Physics and Optoelectronics, Xiangtan University, Xiangtan, 411105, Hunan, China*
[2]*Department of Physics and Astronomy, Rutgers University, Piscataway, New Jersey 08854-8019, USA*

The unique properties of topological semimetals have strongly driven efforts to seek for new topological phases and related materials. Here, we identify a critical condition for the existence of intersecting nodal rings (INRs) in symmorphic crystals, and further classify all possible kinds of INRs which can be obtained in the layered semiconductors with Amm2 and Cmmm space group symmetries. Several honeycomb structures are suggested to be topological INR semimetals, including layered and "hidden" layered structures. Transitions between the three types of INRs, named as α-, β- and γ-type, can be driven by external strains in these structures. The resulting surface states and Landau-level structures, more complicated than those resulting from a simple nodal loop, are also discussed.

Corresponding author: chenyp@xtu.edu.cn

Following the experimental detection of Fermi-arc surface states in Weyl semimetals[1-3], considerable attention has focused on the investigation of topological semimetals/metals (TMs) more generally[4-8]. Classic examples of TMs are the Weyl and Dirac semimetals[9-15], which exhibit twofold and fourfold degenerate Fermi points respectively. These nodal-point semimetals display a number of exotic transport phenomena such as negative magnetoresistance and the chiral magnetic effect[16-19]. Nodal line/ring semimetals belong to another class of TMs[20-27], in which the valence and conduction bands cross along one-dimensional lines in three-dimensional (3D) k-space. In general, the line is not pinned at the Fermi energy[28-30], but passes through the Fermi energy at discrete points. As a consequence, the Fermi surface takes the shape of a thin tube with changing radius, possibly with constrictions. These semimetals are expected to exhibit graphene-like Landau levels and enhanced sensitivity to long-range Coulomb interaction[31-36]. Unlike nodal points, nodal lines/rings can form various topologically connected structures such as chains[37,38], knots[39], and Hopf links[40-42], bringing new physics and topological properties.

On the other hand, two-dimensional materials are the focus of another recently thriving field[43]. After graphene, many graphene-like honeycomb structures have been proposed, and some of them have been fabricated successfully[44-49], including silicene, germanene, BN, and phosphorene. These not only show intrinsic interesting properties in single-sheet form, but also have interesting hybrid properties when stacked into 3D materials[50-52]. These stacked structures often have a mirror symmetry along the stacking direction, and since nodal lines/rings can be protected by mirror

symmetry[53-56], it is natural to ask whether we can obtain topological nodal line/ring semimetals by the stacking of layered structures.

Here we identify a necessary condition for the existence of intersecting nodal lines in symmorphic crystal structures. By stacking semiconducting honeycomb layers, three types of intersecting nodal rings (INRs), as shown in Fig. 1, are found to occur. The α-type consists of isolated crossed rings as in Panel (a), the β-type corresponds to a nodal chain like that in Panel (c), and the γ-type is the structure of ladder of parallel rings as in Panel (d). Moreover, the three topological phases can be converted into one another via application of external strain. Interesting surface states and Landau levels (LLs) in these INR semimetals are discussed. Several 3D layered or "hidden" layered materials are suggested to possess the topological nodal rings. A tight-binding (TB) model is used to explain the relations between the topological phases and how they evolve into one another.

For the INRs to be protected, a critical necessary condition is *the presence of at least two intersecting mirror or glide planes commuting with each other* in the crystal structure[57]. For simplicity, here we consider only two bands (occupied/unoccupied) near the Fermi level in the presence of two mirror planes without spin-orbit coupling. Let us denote the two mirror planes in the momentum space as A and B, as shown in Fig. 1(a). The occupied and unoccupied bands on the AB-intersecting line, say between points X and Y, can be labeled with two mirror eigenvalues $a^{\pm}$ and $b^{\pm}$ taking values ± 1. The right half of Fig. 1(b) shows the bands on the XY-line. If the two bands have eigenvalue pairs (a^{+},b^{+}) and (a^{-},b^{-}) respectively, then they can cross without a gap

opening[58]. If we deviate from the XY-line to look at the bands on a generic k-path residing in plane *A* (see the curved arrow in Fig. 1(a)), then the two bands can cross again because of different *A* eigenvalues for each band, as depicted in the left half of Fig. 1(b). The same argument applies to plane *B*, hence this guarantees the presence of two nodal lines in planes *A* and *B* respectively, meeting at the band crossing point on the XY line and forming a nodal link. Note that non-symmorphic (glide or screws) characters are not mandatory, so this kind of nodal chains can exist even in symmorphic crystals[59-61], in contrast to a previous suggestion where the non-symmorphic nature was essential[37]. Whether the nodal lines are closed or open depends on details of the band dispersion, and the α-type INR can be transformed into β- or γ-type as shown from our following results.

According to the necessary condition of INRs, two structure types are considered (Fig. 2). The first kind consists of 3D layered structures with sp^2-hybridization atoms, as shown in Fig. 1(a), with the planar layers stacked in an AA' stacking sequence (Fig. 2(c)). Each layer consists of hexagonal rings with each ring including two types of atoms labeled A1 and A2. The four-atom primitive cell (two A1 and two A2) is shown in Fig. 2(b). Atoms of the same type form dimers along the armchair direction, while those of opposite type make up the zigzag chains. The second structure type is a porous network in which sp^2-hybridized zigzag chains are connected by sp^3-hybridized linker atoms (Fig. 2(d)). Its primitive cell in Fig. 2(e) includes six (two sp^3 and four sp^2) atoms. Since the bands closest to the Fermi level will be dominated by the sp^2 atoms, it is reasonable to neglect the sp^3-hybridized atoms in a first approximation, in which case

the sp^2 atoms form a structure of buckled layers stacked in an AA' sequence (Fig. 2(f)). The angle θ between lattice vectors is defined in the figures. Both types of structures have two mirrors on the planes *xz* and *xy*.

When only one orbital of each atom in Fig. 2(a) is considered, a 4×4 TB model can be used to describe its electronic properties:

$$H = \sum_i \varepsilon_\alpha a_i^\dagger a_i + \sum_{i,j} t_\beta a_i^\dagger a_j, \quad (1)$$

where $a_i^\dagger / a_j$ represent the creation/annihilation operators, ε_α $(\alpha = 1,2)$ represent site energies of atoms A1 and A2, t_β $(\beta = 1 \ldots 7)$ are the hopping parameters between atoms. Here t_1 to t_5 describe the intra-layer interactions, while t_6 and t_7 describe the inter-layer couplings (Fig. 2(b)). When the sp^3-hybridization atoms in Fig. 2(d) are neglected, the porous network becomes a layered structure. From this point of view, the main difference between the structures of Figs. 2(a) and 2(d) is that the layers in the latter are buckled rather than planar. Because of this close analogy, Eq. (1) can be used to describe the electronic properties of both structures.

We start from a semiconducting single layer. In this case the interlayer interactions in Eq. (1) can be omitted, i.e., we can set $t_6 = t_7 = 0$. The dashed red lines in Fig. 3(a) show the band structure of a typical single-layer semiconductor. It has a substantial band gap, and completely flat bands along paths Z-T, R-T and T-S because of the absence of interlayer couplings. When the semiconducting layers are stacked into a 3D structure, the interlayer couplings t_6 and t_7 become involved. As a result, the flat bands become dispersive, and the conduction and valence bands cross at the Fermi level. In Fig. 3(a) these crossings look like Dirac points, but as we shall see, they link together

in 3D to form nodal rings or lines.

By tuning the parameters in Eq. (1), the three types of INRs in Fig. 1 can be generated. Figure 3(a) presents the band structure for the α-type rings. One can find that there are crossings along Z-T, T-Y, R-T and T-C. In the full Brillouin-zone (BZ), these crossing points lie on two perpendicular nodal rings with a common center at T, as shown in Fig. 3(d). One ring lies on the $k_a = k_b$ plane (plane *A*) while the other lies on the $k_c = 0$ plane (plane *B*). By comparing the band eigenvalues, it can be seen that this pattern corresponds to the α-type phase in Fig. 1(a).

By increasing the intralayer hoppings while decreasing the interlayer ones, the band structure in Fig. 3(a) evolves into that of Fig. 3(b) by inverting occupied/unoccupied bands at C and R points, after which we find crossings along Z-T, T-Y and C-Z. These crossing points lie on two perpendicular INRs on planes $k_a = k_b$ and $k_c = 0$ centered on the points T and Z respectively, as shown in Fig. 3(e). They link in the full BZ and form a nodal chain, corresponding to the β-type phase in Fig. 1(c). This phase is different from the type of nodal chain described in Ref. [36], which is protected by a nonsymmorphic glide-plane symmetry.

By contrast, when the intralayer hoppings are decreased while the interlayer ones are increased, the band structure in Fig. 3(a) evolves into that of Fig. 3(c) by inducing a band inversion at Z. This introduces an additional nodal ring on the *A* plane encircling Z, and the ring on the *B* plane is now open and connects the two rings on plane *A* as shown in Fig. 3(f). The crossing points are now located on the k paths Γ-Z, T-Y, R-T, T-C and C-Z. In the extended BZ the nodal structure has an appearance like a ladder of

parallel rings, corresponding to the γ-type phase in Fig. 1(d). The topological protection of the three types of INRs can also be inferred from their 1D winding numbers along a close path $\mathcal{L}$ encircling the rings: $N_{\mathcal{L}} = \frac{1}{\pi}\oint_{\mathcal{L}} d\boldsymbol{k} \cdot A(\boldsymbol{k})$, where $A(\boldsymbol{k})$ is the Berry connection at the point $\boldsymbol{k}$. The calculation results indicate that all of them have nontrivial values.

To find topological materials possessing these INR phases, we construct structures like Figs. 2(a) and 2(d) based on IV or III/V elements. By calculating band structures using density functional theory (DFT) [62], we find that layered structures BN, AlP and GaP and "hidden" layered structures SiC, BP and BAs can fit the requirements (Fig. S7 in SI). The structural parameters of these structures are shown in Table S1. We calculate their phonon dispersions, and find that there are no soft modes in the spectra of BN and SiC (Fig. S8 in SI). This indicates that BN and SiC are metastable structures having good stability. Therefore, BN and SiC are used as two examples to exhibit the topological properties.

Figure 4(a) shows the band structure of single-layer honeycomb BN, which we find to be a semiconductor with a direct band gap. After the BN layers are stacked into 3D structure by AA' stacking, the band structure changes as shown in Fig. 4(b), which looks quite similar to Fig. 3(a). A close examination indicates that there are indeed α-type nodal rings in BZ. The projections of the band structures illustrate that the states around the Fermi level are contributed mainly by p_z orbitals on B and N atoms. Therefore, it is reasonable that we use Eq. (1) to describe the structures [Detail parameters for fitting the DFT results can be seen in Table S2 in SI].

The band structure of "hidden" layered SiC structure is shown in Fig. 4(c). It is also very similar to the spectrum in Fig. 3(a), and α-type nodal ring is also found here. As mentioned above, the α-type phase evolves into β- and γ-type phases by tuning the hopping energies. An external strain along the direction (110) can induce the same effect as the variation of hopping parameters. As the angle θ changes with the strain from 89º to 80º, meanwhile He atoms are squeezed into the holes of the porous structure[63,64] (the inset in Fig. 4(d)), the band structure changes to that of Fig. 4(d). It is similar to the band spectrum in Fig. 3(c), which means that the system is changed to a β-type nodal-ring semimetal. After θ is increased further from 89º to 108º, the band structure in Fig. 4(e) corresponds to the γ-type nodal ring. As seen from Figs. 4(c-e), all three types of INR structures are accessible for SiC under strain.

Figure 5 presents [010] and $[\bar{1}10]$ surface band structures of the three kinds of INRs. On the [010] surface, we find that all types of INRs exhibit drumhead states inside the projections of the nodal rings (Figs. 5(a-c)). However, the surface states on the $[\bar{1}10]$ surface are different. The surface states of the α-type phase are still drumhead states, as shown in Fig. 5(d). Instead, in the cases of β- and γ-type nodal rings, the linking of the nodal rings induces exotic surface states. In Fig. 5(e), the surface states are distributed in a dumbbell-like region with the two ends corresponding to overlap regions. In Fig. 5(f), the surface state region has the appearance of a donut or an annular eclipse, because the projection of one ring is right in the center of the other. The areas of the surface state regions can be tuned by strain, and the transition between the three types of linked rings can also be tuned.

In search of other types of possible symmetry-allowed INRs, we apply a band representation analysis for our p_z-orbital model [65-73]. Although many different kinds of nodal line structures are allowed, as listed in SI [70], we do find that the α- and β-, and γ-type INRs we presented here are actually an exhausting set of allowed INRs. This is because the formation of nodal intersecting point is not allowed on another mirror-intersecting line Γ-Y, due to the absence of irreducible representations necessary to form the INR. We comment that, a similar analysis on various types of nodal line structures in a non-symmorphic crystal was done in Ref. [73].

One interesting consequence of INRs would be the emergence of flat zeroth LLs in the presence of a magnetic field $\boldsymbol{B}$ applied along the mirror-intersecting line. As discussed in Ref. [74], one should have a set of 2N essentially degenerate zeroth LLs at any given wavevector k along this line, where N is the number of nodal rings spanning the wavevector interval where this k is found. Thus, when there is a chain of β-type INRs connected in k-space, this should yield a flat band of zeroth LLs extending over almost all k, with only small LL gaps opening in the vicinity of the nodal intersections. Electron or hole doping, yielding fully filled or empty zeroth LLs, could lead to a rare realization of the 3D quantum Hall effect[74]. In addition, since the density of states of the zeroth LL varies as a function of angle between the B-field and nodal-ring plane, angular magnetoresistance measurements should be useful in distinguishing between different types of nodal rings[75].

In conclusion, we suggest a generic condition for the presence of INRs and classify them in layered semiconductor materials. These INR semimetals show interesting and

unique transport properties including topological surface states and LLs. Our results suggest a guiding principle to engineer INR semimetals not only in fermionic systems but also in photonics crystals or other bosonic lattices, shedding light on nodal line engineering for further studies.

We thank Jun Won Rhim for his insightful comments. YPC and YEX were supported by the National Natural Science Foundation of China (Nos. 51376005 and 11474243). DV was supported by NSF DMR-1408838 and HSK was supported by NSF DMREF DMR-1629059.

Reference

[1] B. Lv *et al.*, Phys. Rev. X **5**, 031013 (2015).
[2] S. Y. Xu *et al.*, Science **347**, 294 (2015).
[3] S.-Y. Xu *et al.*, Science **349**, 613 (2015).
[4] Q. L. He *et al.*, Science **357**, 294 (2017).
[5] H. Huang, S. Zhou, and W. Duan, Phys. Rev. B **94**, 121117 (2016).
[6] L. Lu, Z. Wang, D. Ye, L. Ran, L. Fu, J. D. Joannopoulos, and M. Soljačić, Science **349**, 622 (2015).
[7] B. Q. Lv *et al.*, Nature (London) **546**, 627 (2017).
[8] A. A. Soluyanov, D. Gresch, Z. Wang, Q. Wu, M. Troyer, X. Dai, and B. A. Bernevig, Nature (London) **527**, 495 (2015).
[9] X. Wan, A. M. Turner, A. Vishwanath, and S. Y. Savrasov, Phys. Rev. B **83**, 205101 (2011).
[10] Z. Wang, Y. Sun, X.-Q. Chen, C. Franchini, G. Xu, H. Weng, X. Dai, and Z. Fang, Phys. Rev. B **85**, 195320 (2012).
[11] Z. Liu *et al.*, Science **343**, 864 (2014).
[12] Z. K. Liu *et al.*, Nat. Mater. **13**, 677 (2014).
[13] Y. Chen, Y. Xie, S. A. Yang, H. Pan, F. Zhang, M. L. Cohen, and S. Zhang, Nano Lett. **15**, 6974 (2015).
[14] H. Weng, C. Fang, Z. Fang, B. A. Bernevig, and X. Dai, Phys. Rev. X **5**, 011029 (2015).
[15] C. Zhong, Y. Chen, Z. M. Yu, Y. Xie, H. Wang, S. A. Yang, and S. Zhang, Nat. Commun. **8**, 15641 (2017).
[16] D. Son and B. Spivak, Phys. Rev. B **88**, 104412 (2013).
[17] X. Huang *et al.*, Phys. Rev. X **5**, 031023 (2015).
[18] F. Arnold *et al.*, Nat. Commun. **7**, 11615 (2016).
[19] H. Li, H. He, H. Z. Lu, H. Zhang, H. Liu, R. Ma, Z. Fan, S. Q. Shen, and J. Wang, Nat. Commun. **7**, 10301 (2016).
[20] A. Burkov, M. Hook, and L. Balents, Phys. Rev. B **84**, 235126 (2011).
[21] L. Lu, L. Fu, J. D. Joannopoulos, and M. Soljačić, Nat. Photon. **7**, 294 (2013).
[22] C. Fang, Y. Chen, H.-Y. Kee, and L. Fu, Phys. Rev. B **92**, 081201 (2015).
[23] Y. Kim, B. J. Wieder, C. L. Kane, and A. M. Rappe, Phys. Rev. Lett. **115**, 036806 (2015).
[24] R. Yu, H. Weng, Z. Fang, X. Dai, and X. Hu, Phys. Rev. Lett. **115**, 036807 (2015).
[25] H. Huang, J. Liu, D. Vanderbilt, and W. Duan, Phys. Rev. B **93**, 201114 (2016).
[26] J. T. Wang, H. Weng, S. Nie, Z. Fang, Y. Kawazoe, and C. Chen, Phys. Rev. Lett. **116**, 195501 (2016).
[27] G. Chang, S. Y. Xu, X. Zhou, et al., Phys. Rev. Lett. **119**, 156401 (2017).
[28] G. Xu, H. Weng, Z. Wang, X. Dai, and Z. Fang, Phys. Rev. Lett. **107**, 186806 (2011).
[29] L. M. Schoop *et al.*, Nat. Commun. **7**, 11696 (2016).
[30] Q. Xu, R. Yu, Z. Fang, X. Dai, and H. Weng, Phys. Rev. B **95**, 045136 (2017).
[31] J. González, F. Guinea, and M. Vozmediano, Phys. Rev. Lett. **77**, 3589 (1996).
[32] V. N. Kotov, B. Uchoa, V. M. Pereira, F. Guinea, and A. H. Castro Neto, Rev. Mod.

Phys. **84**, 1067 (2012).
[33] S.-K. Jian and H. Yao, Phys. Rev. B **92**, 045121 (2015).
[34] H.-H. Lai, Phys. Rev. B **91**, 235131 (2015).
[35] J.-W. Rhim and Y. B. Kim, Phys. Rev. B **92**, 045126 (2015).
[36] Y. Huh, E.-G. Moon, and Y. B. Kim, Phys. Rev. B **93**, 035138 (2016).
[37] T. Bzdusek, Q. Wu, A. Ruegg, M. Sigrist, and A. A. Soluyanov, Nature (London) **538**, 75 (2016).
[38] Z. Yan and Z. Wang, Phys. Rev. B **96**, 041206 (2017).
[39] M. Ezawa, Phys. Rev. B **96**, 041202 (2017).
[40] P.-Y. Chang and C.-H. Yee, arXiv:1704.01948.
[41] W. Chen, H.-Z. Lu, and J.-M. Hou, Phys. Rev. B **96**, 041102 (2017).
[42] Z. Yan, R. Bi, H. Shen, L. Lu, S.-C. Zhang, and Z. Wang, Phys. Rev. B **96**, 041103 (2017).
[43] K. S. Novoselov, A. K. Geim, S. V. Morozov, D. Jiang, Y. Zhang, S. V. Dubonos, I. V. Grigorieva, and A. A. Firsov, Science **306**, 666 (2004).
[44] M. E. Dávila, L. Xian, S. Cahangirov, A. Rubio, and G. Le Lay, New J. Phys. **16**, 095002 (2014).
[45] D. Hanlon *et al.*, Nat. Commun. **6**, 8563 (2015).
[46] G. Lu, T. Wu, Q. Yuan, H. Wang, H. Wang, F. Ding, X. Xie, and M. Jiang, Nat. Commun. **6**, 6160 (2015).
[47] P. Vogt, P. De Padova, C. Quaresima, J. Avila, E. Frantzeskakis, M. C. Asensio, A. Resta, B. Ealet, and G. Le Lay, Phys. Rev. Lett. **108**, 155501 (2012).
[48] J. L. Zhang *et al.*, Nano Lett. **16**, 4903 (2016).
[49] F. F. Zhu, W. J. Chen, Y. Xu, C. L. Gao, D. D. Guan, C. H. Liu, D. Qian, S. C. Zhang, and J. F. Jia, Nat. Mater. **14**, 1020 (2015).
[50] J. Hass, W. A. de Heer, and E. H. Conrad, J. Phys. Condens. Mat. **20**, 323202 (2008).
[51] J. Qiao, X. Kong, Z. X. Hu, F. Yang, and W. Ji, Nat. Commun. **5**, 4475 (2014).
[52] Z. Zhu and D. Tomanek, Phys. Rev. Lett. **112**, 176802 (2014).
[53] G. Bian *et al.*, Nat. Commun. **7**, 10556 (2016).
[54] G. Bian *et al.*, Phys. Rev. B **93**, 121113 (2016).
[55] Y. H. Chan, C.-K. Chiu, M. Y. Chou, and A. P. Schnyder, Phys. Rev. B **93**, 205132 (2016).
[56] J. Zhao, R. Yu, H. Weng, and Z. Fang, Phys. Rev. B **94**, 195104 (2016).
[57] These considerations can also be generalized to non-symmorphic systems with intersecting glide and/or mirror planes. If these two operations anticommute with each other, however, a twofold degeneracy is enforced on the line instead of a band crossing at one point.
[58] A similar scenario applies to a crossing between bands (a^+,b^-) and (a^-,b^+).
[59] H. Weng, Y. Liang, Q. Xu, R. Yu, Z. Fang, X. Dai, and Y. Kawazoe, Phys. Rev. B **92**, 045108 (2015).
[60] T. Kawakami and X. Hu, arXiv:1611.07342.
[61] R. Yu, Q. Wu, Z. Fang, and H. Weng, arXiv:1701.08502.
[62] See SI for further details of our calculations, which includes Refs. [76-77].
[63] N. V. Krainyukova and E. N. Zubarev, Phys. Rev. Lett. 116, 055501 (2016).
[64] J. A. Venables and D. J. Ball, Proc. R. Soc. A 322, 331 (1971).

[65] B. Bradlyn, L. Elcoro, J. Cano, M. G. Vergniory, Z. Wang, C. Felser, M. I. Aroyo, and B. A. Bernevig, Nature 547, 298 (2017).
[66] M. G. Vergniory, L. Elcoro, Z. Wang, J. Cano, C. Felser, M. I. Aroyo, B. A. Bernevig, and B. Bradlyn, Phys. Rev. E 96, 023310 (2017).
[67] B. Bradlyn, L. Elcoro, M. G. Vergniory, J. Cano, Z. Wang, C. Felser, M. I. Aroyo, and B. A. Bernevig, arXiv:1709.01937 (2017).
[68] J. Cano, B. Bradlyn, Z. Wang, L. Elcoro, M. G. Vergniory, C. Felser, M. I. Aroyo, and B. A. Bernevig, arXiv:1709.01935 (2017).
[69] L. Elcoro, B. Bradlyn, Z. Wang, M. G. Vergniory, J. Cano, C. Felser, B. A. Bernevig, D. Oroben-Goa, G. de la Flor, and M. I. Aroyo, J. of Appl. Crystallogr. 50, 1457 (2017).
[70] See SI for a heuristic introduction about the band representations and the different kinds of nodal structures allowed under the *Amm2* and *Cmmm* space groups.
[71] J. Zak, Phys. Rev. Lett. 45, 1025 (1980).
[72] H. Bacry, L. Michel, and J. Zak, Phys. Rev. Lett. 61, 1005 (1988).
[73] A. Bouhon and A. M. Black-Schaffer, arXiv:1710.04871 (2017). For the band representation analysis, we used BANDREP code recently implemented in Bilbao Crystallographic Server (http://www.cryst.ehu.es).
[74] J. W. Rhim and Y. B. Kim, Phys. Rev. B 92, 045126 (2015).
[75] Whether the density of state of the zeroth LL merely becomes zero or the LL fully gaps depends on the choice of model. See Ref. [65] where the zeroth LL remains gapless at a point, and Ref. [37] with the fully gapped LL except at a specific magnetic field strength.
[76] G. Kresse and J. Hafner, Phys. Rev. B 47, 558 (1993).
[77] J. P. Perdew, K. Burke, and M. Ernzerhof, Phys. Rev. Lett. 77, 3865 (1996).

Figure captions

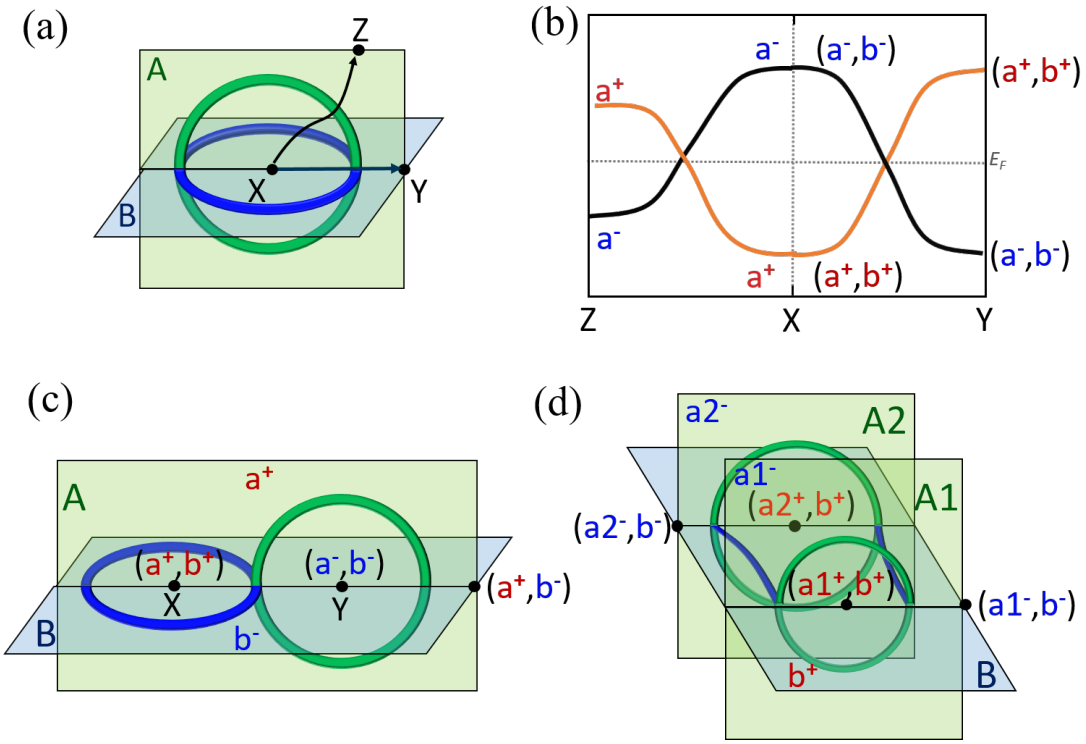

Figure 1. (color online) (a) An α-type INR, and (b) a simple model band structure manifesting nodal links from the two mirror symmetries *A* and *B* in (a). The right and left halves of (b) correspond to the bands on the k-path X-Y (straight arrow in (a)) and X-Z (curved black arrows), respectively. Different color (red and blue) represents different symmetry eigenvalues. (c) β -type and (d) γ -type INRs. Symmetry eigenvalues of the occupied band are shown in (a), (c) and (d).

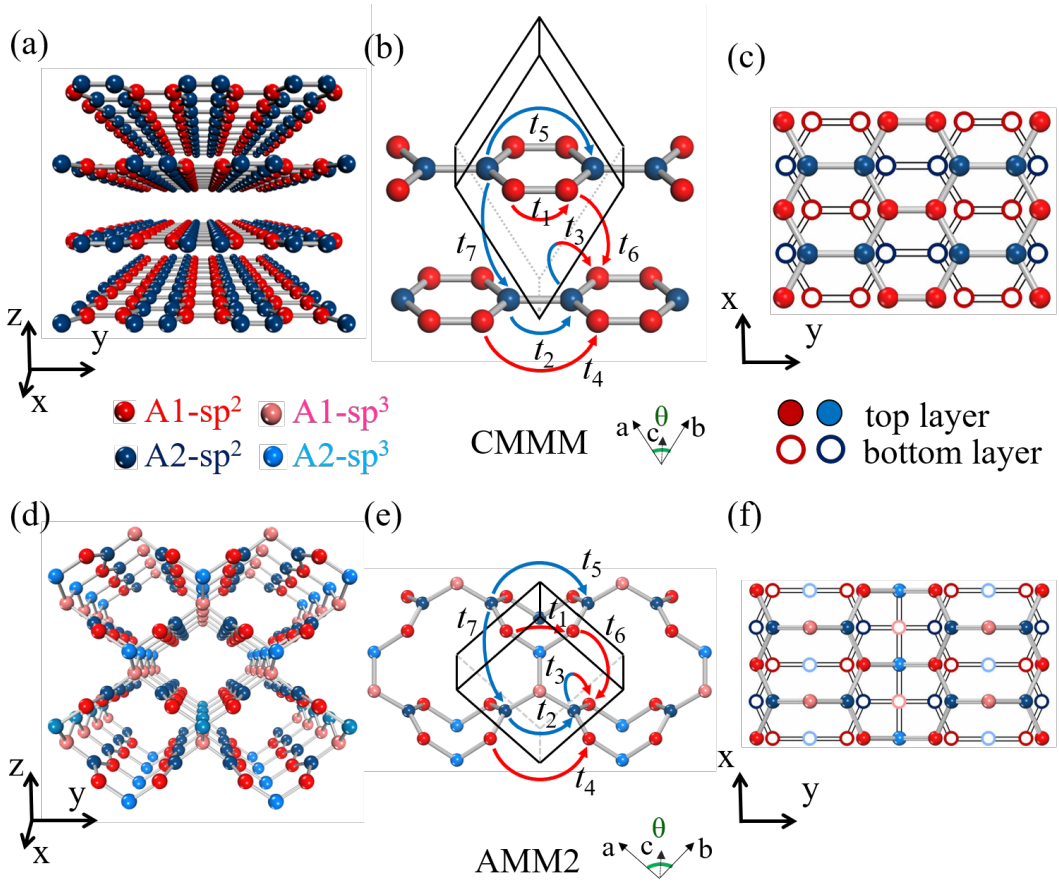

Figure 2. (color online) AA' stacked honeycomb layered structure (a), its primitive cell (b) and top view (c). "Hidden" AA' stacked honeycomb layered network (d), its primitive cell (e) and top view (f). Both of the structures are made of two kinds of atoms A1 and A2. t_1~t_7 in (b) and (e) describe the hopping parameters of the structures.

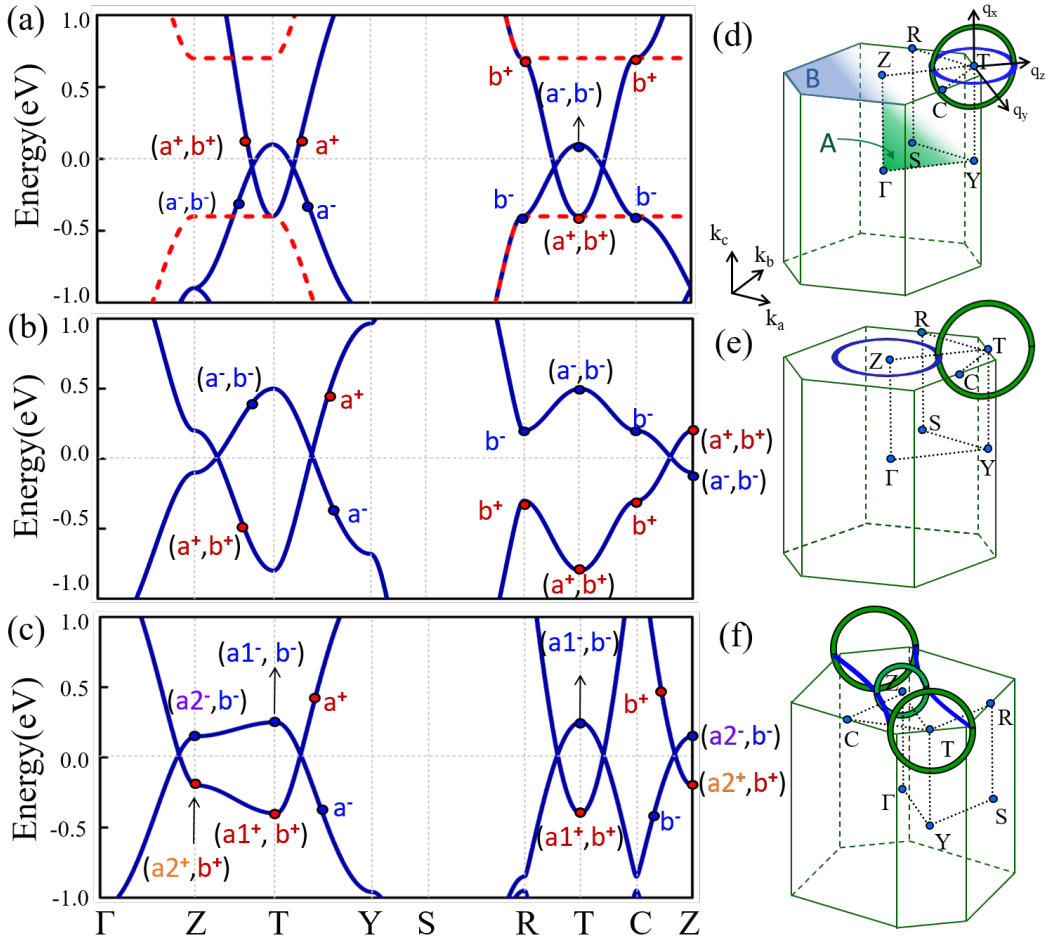

Figure 3. (color online) Band structures based on Eq. (1) with different parameters: (a) t_1=-1, t_2=-0.5, t_3=-1.2, t_4=t_5=0, t_6=0.55, t_7=0.25; (b) t_1=-2.0, t_2=-1.1, t_3=-1.2, t_4=t_5= 0, t_6=0.25, t_7=0.15; (c) t_1=-0.1, t_2=-0.05, t_3=-1.2, t_4=t_5=0, t_6=1.0, t_7=0.55. Other parameters are ε_1=1.7, ε_2=-0.9. All the values are in units of eV. Red dashed line in (a) depicts band structure for a single-layer semiconducting with the same parameters as (a) but t_6=t_7=0. (d-f) Arrangements of the topological INRs in reciprocal space corresponding to the band structures in (a-c) respectively. In (a-c), eigenvalues for A- and B-mirror planes are shown, where the two mirror planes are illustrated in (d). Note that, in (f), the A-eigenvalues at T and Z are denoted in different symbols ($a1^{\pm}$ and $a2^{\pm}$ respectively), and the BZ is different from (d-e) because of changed unit cell parameters, which is used to mimic the DFT results discussed later.

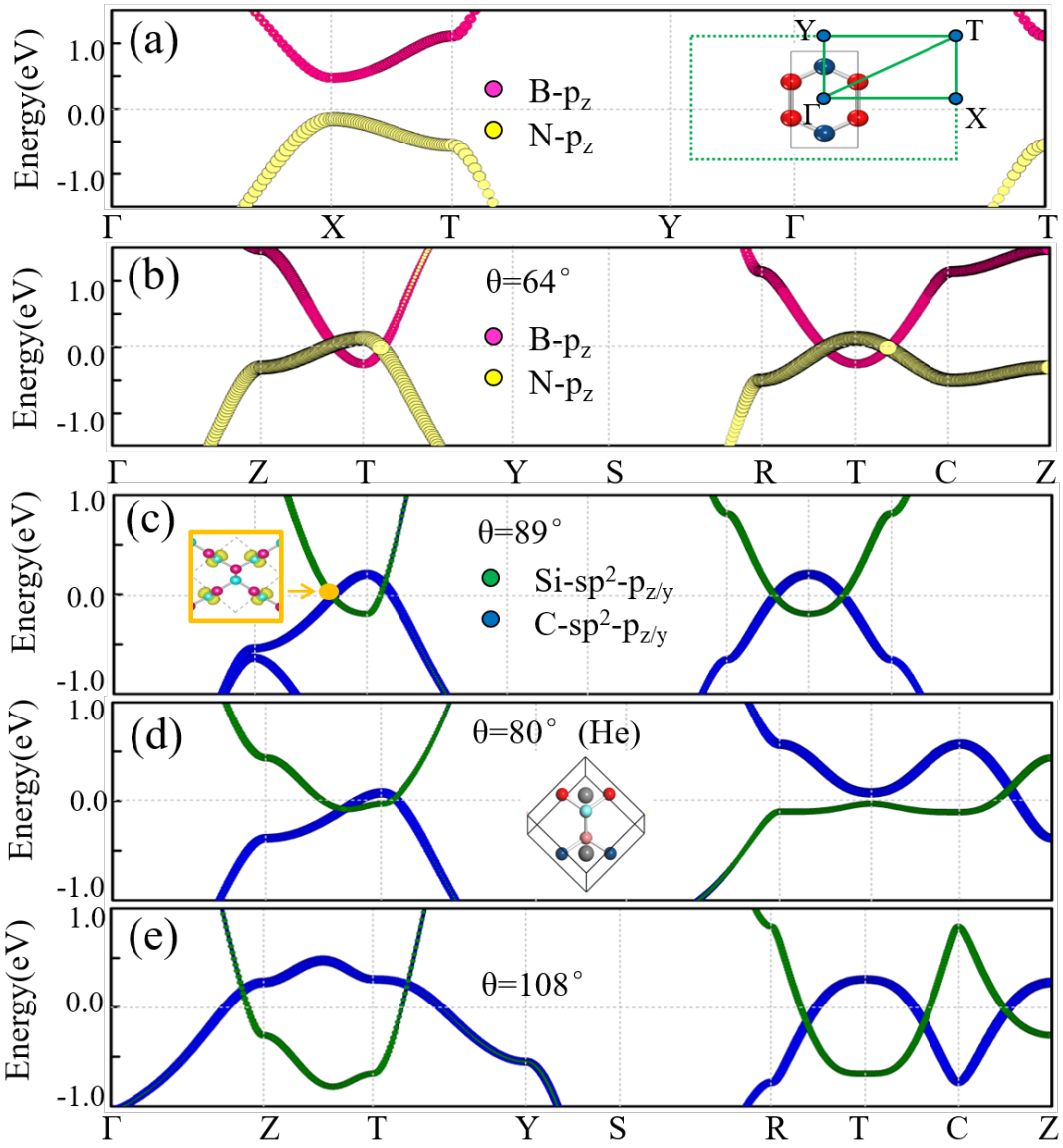

Figure 4. (color online) Projected band structures of (a) single-layer and (b) stacked 3D layered BN (Fig. 1(a)). Projected band structures of "hidden" layered structure SiC with $\theta = 89^0$ (c), 80^0 (d) and 108^0 (e). Insets: (c) charge density of a state around the nodal point, indicating the bonds are similar to the π bonds in graphene; (d) a primitive cell of SiC where He atoms are inserted into the holes.

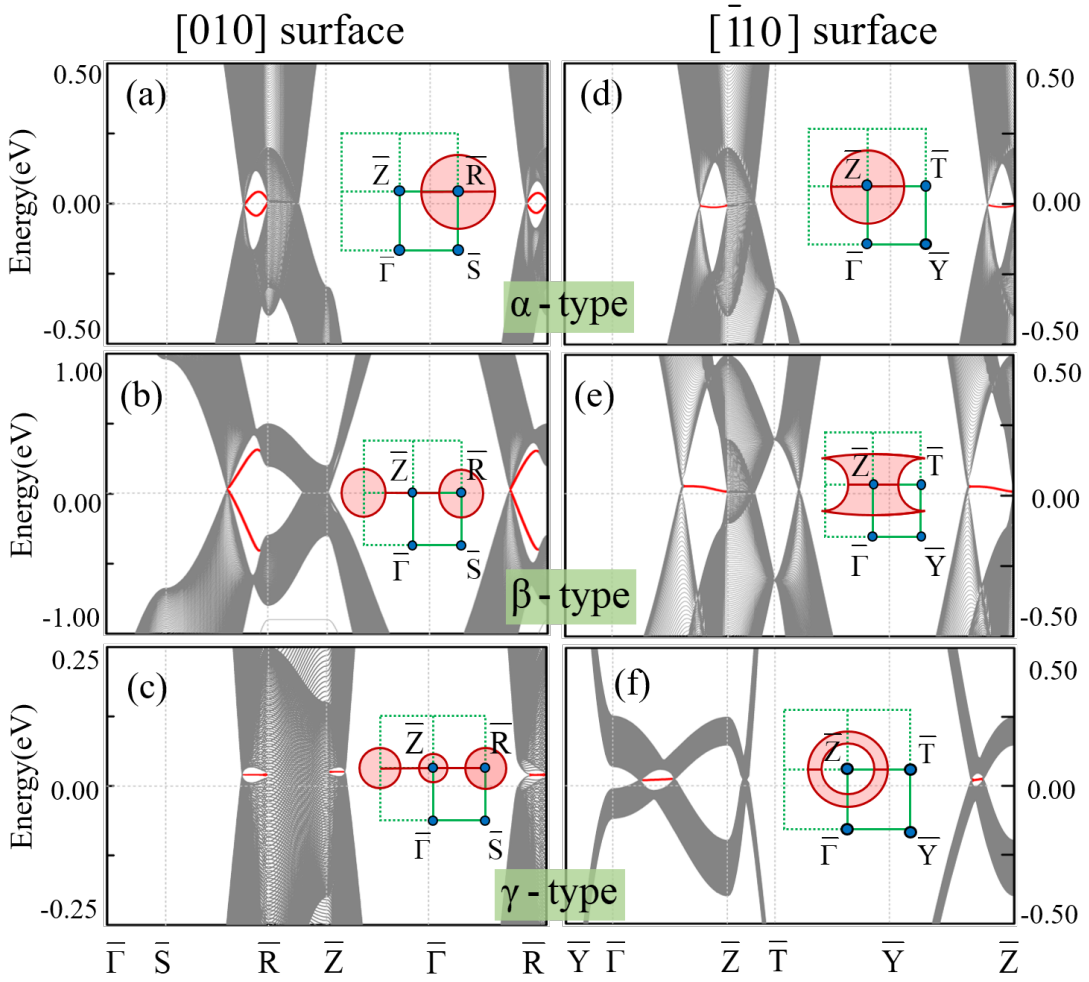

Figure 5. (color online) (a-c) Topological surface states for α-, β- and γ-type LNRs, respectively, on the [$\bar{1}$10] surface. Insets show the surface states regions (red shadows) in the BZ. (d-f) Same but for the [$\bar{1}$10] surface. Because the [010] slabs are terminated by two different surfaces, two different surface states appear in (a-c). However, the surfaces of [$\bar{1}$10] slabs are the same, and thus the two surface states in (d-f) are degenerate.

Supplementary Information for

"Symmorphic intersecting nodal rings in semiconducting layers"

Cheng Gong,[1] Yuee Xie,[1] Yuanping Chen,[1] Heung-Sik Kim,[2] and David Vanderbilt[2]

[1]*School of Physics and Optoelectronics, Xiangtan University, Xiangtan, 411105, Hunan, China*

[2]*Department of Physics and Astronomy, Rutgers University, Piscataway, New Jersey 08854-8019, USA*

CONTENTS

I. BAND REPRESENTATION ANALYSES FOR LAYERED AND BUCKLED HONEYCOMB STRUCTURES

A. An introduction to band representation analysis

Here we denote nodal rings touching each other as *intersecting nodal rings* (INRs), rings winding each other as *Hopf links*, and those with neither intersecting nor forming Hopf links as *separate nodal rings*. In the INR case, the point where the two nodal line cross will be denoted as the *nodal intersecting point*. Also, we use 'IRREP' as a shorthand notation for 'irreducible representation.'

In the manuscript we showed that INRs can exist when there are two (or more) mirror planes intersecting each other, so that the nodal intersecting point exists on the mirror-intersecting line. This suggests that we may also have additional INRs with nodal intersecting points located on the other mirror-intersecting line Γ-Y (see Fig. 3(d-f) in the manuscript for the special points notation), which were not found in the tight-binding and *ab-initio* calculations. It can be seen that, by employing a *band representation* (BR) analysis, nodal intersecting points can exist only on the Z-T line when we are considering only the p_z-orbitals at sp^2-bonded sites, so that our listing of INR structures in Fig. 3 covers all possible INR cases. This is because the *symmetries of the local orbitals underlying the band structure determines the kind and number of IRREPs in the entire momentum space*.

Before describing these results, we describe below what a BR analysis is in a hand-waving manner. For a mathematically rigorous presentation please refer to Refs. 1–4 and references therein.[5] Basically, it is a momentum-space representation of a space group. We know well about the representation theory of little co-groups (which are point groups) at high-symmetry k-points, which tells us how many different kinds of degenerate states (*i.e.*, IRREPs) we can have for each k-point. On the other hand, from the number of local orbitals and number of sites in our choice of unit cell, we know how many bands we will have in our tight-binding model. BR theory is, roughly speaking, the combination of these two ideas; choosing our set of sites and local orbitals from which we will construct our model, we can explicitly write the the representation of each space group operation in terms of a local-orbital basis in real space (which becomes an infinite-dimensional unitary matrix) and then do the Fourier transform to obtain a k-space representation. Among the original space-group operations, we can choose a little group of a lower-symmetry k-point (*i.e.*, 'subducing' the representation) and find which kind of IRREPs we have at that point. Furthermore, for any

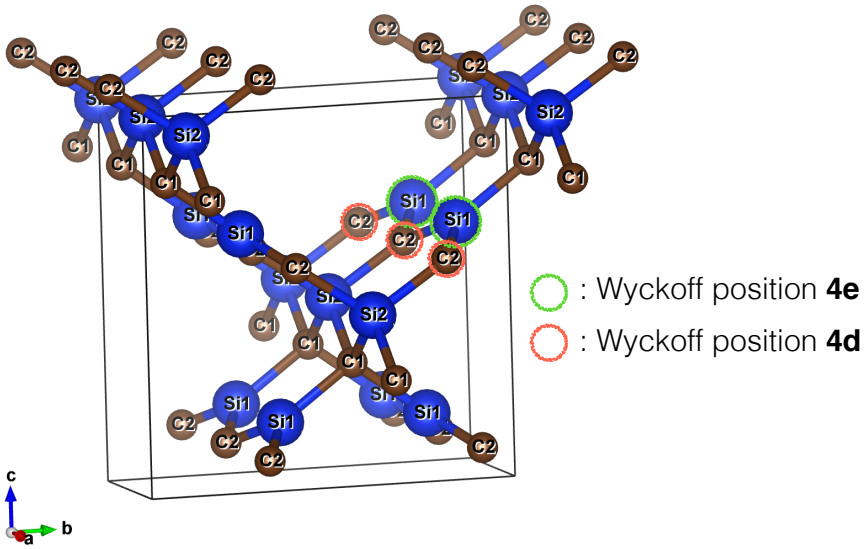

FIG. S1. (color online) Crystal structrue of buckled honeycomb SiC with $Amm2$ space group. p_z-like orbitals at Si1 and C2 sites, highlighted with green (Wyckoff position 4e) and pink (4d) circles respectively, contributes to the bands near the Fermi level.

high-symmetry lines connecting two points with even higher symmetry, we can find '*compatibility relations*' telling us about how each IRREP on one higher-symmetry point is connected to IRREPs on another point through the line connecting the two points. From this analysis the connectivity of high-symmetry IRREPs to form a band structure can be obtained, and the nodal ring structure can also be deduced.

B. Choice of local orbitals in buckled honeycomb SiC (space group $Amm2$)

Below we apply the BR theory to a simple example, the buckled honeycomb SiC with the $Amm2$ space group symmetry discussed in the manuscript. Note that the BR analysis employed in this $Amm2$ example can be applied to the layered honeycomb structure with the $Cmmm$ symmetry to yield the same conclusion as presented in Sec. I E. Here we do not consider the effect of SOC, which gaps out all nodal lines and drives the system either to a weak or strong topological insulator.[6] Fig. S1 shows the crystal structure of SiC with $Amm2$ symmetry in a conventional setting, where there are two mirror planes perpendicular to $\mathbf{a}$ (denoted $m_{\rm A}$) and to $\mathbf{b}$ ($m_{\rm B}$). In the primitive cell there are four different symmetry-inequivalent sites: C1 and Si2 with C_{2v} site symmetry, and C2 and Si1 with lower C_s symmetry associated with $m_{\rm A}$ only. Since C1 and Si2 sites are sp^3-bonded, we choose instead to explore the bands induced from the p_z-like orbitals at

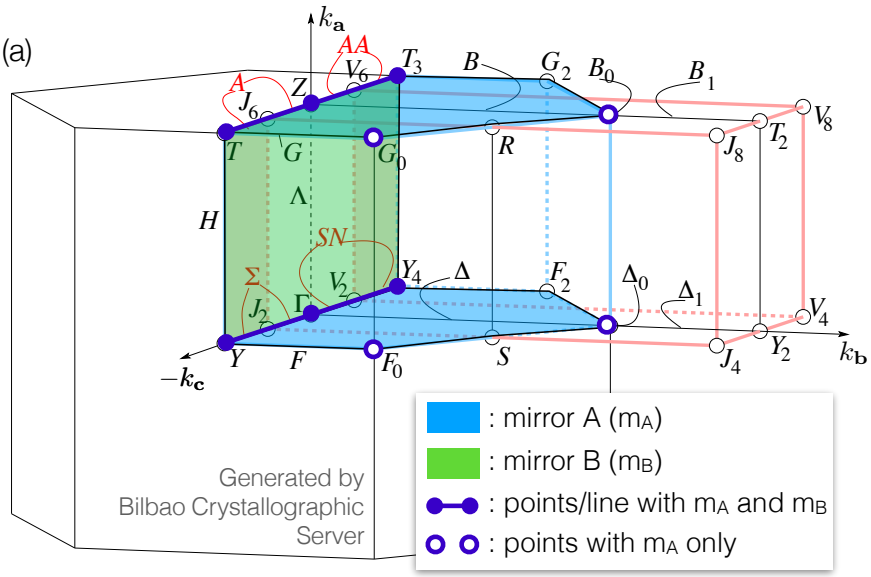

(b) from C2 (WP 4d)

Band-Rep.	A'↑G(2)
Band-type	Composite
Z:(1/2,0,0)	$Z_1(1) \oplus Z_4(1)$
T:(1/2,0,-1)	$T_1(1) \oplus T_4(1)$
R:(1/2,1/2,-1/2)	$2\,R_1(1)$
S:(0,1/2,-1/2)	$2\,S_1(1)$
Y:(0,0,-1)	$Y_1(1) \oplus Y_4(1)$
Γ:(0,0,0)	$Γ_1(1) \oplus Γ_4(1)$

(c) from Si1 (WP 4e)

Band-Rep.	A'↑G(2)
Band-type	Composite
Z:(1/2,0,0)	$Z_2(1) \oplus Z_3(1)$
T:(1/2,0,-1)	$T_2(1) \oplus T_3(1)$
R:(1/2,1/2,-1/2)	$2\,R_2(1)$
S:(0,1/2,-1/2)	$2\,S_1(1)$
Y:(0,0,-1)	$Y_1(1) \oplus Y_4(1)$
Γ:(0,0,0)	$Γ_1(1) \oplus Γ_4(1)$

Tables generated by BANDREP in Bilbao Crystallographic Server

FIG. S2. (color online) (a) Brillouin zone and high-symmetry planes of $Amm2$ structure, where m_{A} and m_{B} are perpendicular to the **a** and **b** axes in Fig. 1 respectively. Note that B_0, G_0, Δ_0, and F_0 has only m_{A} symmetry. (b,c) Tables of BRs generated from Wyckoff position 4d (b) and 4e (c). Note that C2 (shown in Fig. 1) and Si1 are located at 4d and 4e sites respectively. In both tables, grey rectangles highlight BRs induced from p_z-like orbitals (A' IRREP of C_s site symmetry, symmetric upon m_{A} operation, at both 4d and 4e sites).

the C2 and Si1 sites, which are nearer to the Fermi level.

To construct the BRs, we start from the p_z-like orbitals (A' IRREP, symmetric upon m_{A}) at C2 and Si1 sites with C_s point group symmetry. Using the BANDREP program recently implemented in the Bilbao Crystallographic Server,[7,8] we can generate BRs as shown in Fig. S2(b) and (c). In the tables, the first row shows which local IRREP we chose to construct the BR. Here we

are interested in bands consisting of A' IRREP (p_z-like orbitals) at 4d (b) and 4e (c) Wyckoff sites. The 'composite' band-type in the second row means that the two bands generated can be separated into two 'elementary' sets of BRs with a constant energy shift of each subband, where elementary BRs (EBRs) are defined as BRs induced from IRREPs at Wyckoff positions with maximal site symmetry. In spinless systems it has been shown that EBRs are indecomposable,[9,10] *i.e.* an EBR cannot be decomposed into two sets of smaller BRs separated by a band gap. Note that $Amm2$ symmetry allows only one-dimensional EBRs in the absence of spin. Lastly, the third and subsequent rows in the tables show which IRREPs exist at six high-symmetry points (Z, T, R, S, T, and Γ), where the BZ and high-symmetry k-points are shown in Fig. S2(a). Note that the Z-T and Γ-Y lines are mirror-intersecting lines with C_{2v} symmetry, so they can host four one-dimensional IRREPs $\{\text{Z,T,Y,}\Gamma\}_{1,\cdots,4}$, while points R and S have only two IRREPs $\{\text{R,S}\}_{1,2}$ from their C_s symmetry. Also note that, in Fig. S2(a), point R (S) has the same symmetry with B_0 and G_0 (Δ_0 and F_0).

C. Compatibility relation between high-symmetry k-points

Since we know how many different IRREPs we have in our system, we now need to connect them to form the band structures. BANDREP provides the information about the connectivity (i.e., the compatibility relations), so that one can simply use them, but here we want to be a bit more illustrative. The compatibility relations between different IRREPs is determined by how IRREPs at higher-symmetry points are reduced into IRREPs with lower symmetries, deduced from their symmetry eigenvalues. Eigenvalues of m_{A} and m_{B} for each IRREP at different k-points are as

follows;

	m_{A}	m_{B}
$\{Z,T,Y,\Gamma\}_1$	$+$	$+$
$\{Z,T,Y,\Gamma\}_2$	$-$	$-$
$\{Z,T,Y,\Gamma\}_3$	$-$	$+$
$\{Z,T,Y,\Gamma\}_4$	$+$	$-$
$\{B_0,G_0,\Delta_0,F_0\}_1$	$+$	$\cdot$
$\{B_0,G_0,\Delta_0,F_0\}_2$	$-$	$\cdot$
Λ_1	$\cdot$	$+$
Λ_2	$\cdot$	$-$

(S1)

where Λ denotes a generic point on the m_{B} plane in Fig. S2(a). From this, we know that $\{$Z,T,Y,$\Gamma\}_{1,4}$ are connected to $\{$B$_0$,G$_0$,Δ_0,F$_0\}_1$ and $\{$Z,T,Y,$\Gamma\}_{2,3}$ to $\{$B$_0$,G$_0$,Δ_0,F$_0\}_2$ when we deviate from the mirror-intersecting line but stay in the m_{A} plane. Similarly, $\{$Z,T,Y,$\Gamma\}_{1,3}$ and $\{$Z,T,Y,$\Gamma\}_{2,4}$ are connected to Λ_1 and Λ_2, respectively, in the m_{B} plane.

D. Possible band structures and nodal lines in SiC

Now we are ready to generate possible set of band structures from the sp^2-bonded sites in buckled SiC. A couple of remarks are worth mentioning for further simplification of our analysis; *i)* Unlike other high-symmetry points, the points on the m_{A} plane with k_x = 0 (represented by S) host only a single IRREP S$_1$ as shown in Fig. S2(b) and (c), implying we do not have any protected band crossing on the plane. *ii)* From the symmetry argument in the manuscript, we know that nodal intersecting points can only happen on the mirror-intersecting lines and when two IRREPs with two opposite eigenvalues cross each other. Denoting the IRREPs at generic k-points on the mirror-intersecting Z-T and Γ-Y lines as $\overline{\mathrm{ZT}}_{1,\cdots,4}$ and $\overline{\Gamma\mathrm{Y}}_{1,\cdots,4}$, respectively, we can have nodal intersecting points when $\{\overline{\mathrm{ZT}},\overline{\Gamma\mathrm{Y}}\}_1$ and $\{\overline{\mathrm{ZT}},\overline{\Gamma\mathrm{Y}}\}_2$ (or $\{\overline{\mathrm{ZT}},\overline{\Gamma\mathrm{Y}}\}_3$ and $\{\overline{\mathrm{ZT}},\overline{\Gamma\mathrm{Y}}\}_4$) cross on the mirror-intersecting lines. While we have all four IRREPs on the Z-T line, on the contrary, we have only two IRREPs $\overline{\Gamma\mathrm{Y}}_{1,4}$ on the Γ-Y line, implying that we cannot have nodal intersecting points on the Γ-Y line. This is a crucial distinction between the two mirror-intersecting lines that will have important consequences shortly.

With the IRREPs at high-symmetry points in Fig. S2 and the compatibility relations in Table

(S1), the qualitative nature of the band dispersion is determined by the energy ordering of IRREPs. Assuming for simplicity that the dispersions are monotonic along a line segment connecting two high-symmetry points in the BZ, the band structure is determined by energy ordering of IRREPs at six k-points, Z, T, Y, Γ, B_0, and G_0 (since no crossing can exist on the m_A plane with $k_{\mathbf{a}}$, the plane containing the S point). Because there are four 1D IRREPs at Z and T, two 1D IRREPs at Y, Γ, B_0, and G_0, and four bands in total, the number of all possible band structures are $(4!)^2 \left(\frac{4!}{2^2}\right)^4 = 746496$, so generating all of the bands is neither possible nor necessary. Hence, below we will discuss a few illustrative examples about how different kinds of nodal ring structures (separated, INR, and Hopf link) can be generated from our 4-band model. Note that similar but more elaborate analysis was done by Bouhon and Black-Schaffer for space group $Pna2_1$ (SG #33),[11] where the number of possible band structures is greatly reduced by the degeneracy enforced by the three perpendicular screw axes.

1. *NLs involving two bands*

First we consider situations with only two bands crossing at the Fermi level. For simplicity, here we assume that the other two bands are away from the Fermi level (one occupied, another unoccupied) and do not cross with others as shown in Fig. S3. Hereafter we consider half-filling (2 bands occupied), and because we have time-reversal (TR) symmetry, only high-symmetry planes and lines in the TR-irreducible section in the BZ will be depicted.[12]

Fig. S3(a) shows bands with NL crossing on the m_B plane. Here we are depicting bands contributing and not contributing to the NLs as solid and dotted lines, respectively. In Fig. S3(a), we chose that only bands induced from the 4d Wyckoff position (C2) are crossing near the Fermi level, while the bands from the 4e sites (Si1) are away from the Fermi level. Note that when we are making only the solid bands cross, we may have NLs only on the m_B plane since $\{\overline{\mathrm{ZT}},\overline{\Gamma\mathrm{Y}}\}_{1,4}$ have the same m_A eigenvalue. Since no degeneracy is enforced at any k-points, the open NL can be freely deformed into a closed nodal ring or even be removed without any symmetry breaking. Similarly, it is easy to see that we get an identical result when we have two bands from the 4e sites near the Fermi level.

Fig. S3(b) and (c) show the band crossings, choosing one 4d-induced band and another from 4e-induced ones. Fig. S3(b) shows bands with a NL only on the m_A plane, while Fig. S3(c) shows the β-type INR. By comparing Fig. S3(a-c), we can see that the mirror eigenvalues of the IRREPs

crossing on the mirror-intersecting Z-T line determines the presence of NLs on each mirror plane, as discussed above and in the manuscript.

2. *NLs involving three bands*

Now we discuss the band crossings involving three bands. As shown in Fig. S4, we can introduce two separate NLs without sharing the mirror-intersecting Z-T line by combining band crossings depicted in Fig. S3(a) and (b). On the contrary, when we want to make the two NLs share the mirror intersecting line to form INR or Hopf link, as shown in Fig. S5, then we need to cross IRREPs with two opposite eigenvalues on the Z-T line ($\overline{\mathrm{ZT}}_1$ and $\overline{\mathrm{ZT}}_2$, or $\overline{\mathrm{ZT}}_3$ and $\overline{\mathrm{ZT}}_4$). We mention that, this condition is similar with the one presented in Ref. 13, where the transformation of two separate nodal rings into a Hopf link is shown in a four-band model with three distinct IRREPs on the mirror-intersecting line. Unlike their model, however, in Fig. S5 we are considering situations with only three bands with distinct IRREPs are crossing on the mirror-intersecting line. Because of this, it is not possible to transform two separate NLs into a Hopf link by inverting bands only on the Z-T line, which is evident by comparing Fig. S5 (b) and (c).

3. *NLs involving four bands*

Finally we discuss situations where all the 4 bands are contributing to the NL crossings. Fig. S6(a) shows the γ-type nodal intersecting points, while Fig. S6(b) depicting two NLs on the m_{A} plane. Note that both in Fig. S6(a) and (b), by shifting the NL crossing points on the Z-T line, they can overlap at a same point so that all the NLs (4 in (a), 2 in (b)) are connected. However this is just an accidental crossing by a fine-tuning of parameters so may not be physically relevant.

E. Band representations for layered honeycomb (space group $Cmmm$)

In the manuscript, we discuss the layered honeycomb structures with the $Cmmm$ space group in addition to the buckled honeycomb structures. Because the inversion symmetry is present in $Cmmm$ in addition to all the operations in $Amm2$, it has three mirror planes perpendicular to each other. Since there exist more mirror-intersecting lines in the momentum space compared to the $Amm2$ structure, we might have additional nodal intersecting points on different mirror-

intersecting lines to form even more complicated nodal structures. Inducing the band representation from the p_z orbitals at each site and looking into the allowed IRREPs on the lines, however, it turns out that there is only one line, the Z-T line, accommodating IRREPs which can form the nodal intersecting points. Hence the presence of the additional mirror plane in the $Cmmm$ structure (compared to the $Amm2$ one) does not change our conclusion that the three types of INR (α-, β-, and γ-type) exhaust all possible kind of INRs in our layered and buckled honeycomb structures.

II. A $k \cdot p$ MODEL FOR THE THREE TYPES OF INRS

Comparing the four-band TB model in Eq. (1) in the manuscript, we can construct a two-band $k \cdot p$ model to further compare the INRs. All the three types of INRs have a common nodal ring centered on the point T (see Figs. 3(d-f) in the manuscript). Constrained by the symmetries and the time reversal symmetry for a spinless system, one obtains a model up to quadratic order in k around T as

$$H(\mathbf{q}) = \begin{pmatrix} A_1 q_x^2 + B_1 q_y^2 + C_1 q_z^2 & -iDq_x q_y \\ iDq_x q_y & \Delta + A_2 q_x^2 + B_2 q_y^2 + C_2 q_z^2 \end{pmatrix}$$

where $q_i = k_i - k_{i0}$ ($i = x, y, z$) and (k_{x0}, k_{y0}, k_{z0}) is the momentum coordinate at point T. The parameters Δ, $\{A, B, C\}_{\{1,2\}}$, and D are determined by fitting DFT or TB results. When $\{A, B, C\}_1 > 0$ and $\{A, B, C\}_2 < 0$, it produces an α-type INR; when $A_1, B_2, C_1 > 0$ and $A_2, B_1 C_2 < 0$, a β-type-like INR is produced, in which a nodal ring linked two curved nodal lines; when $A_1, C_1 > 0$, $A_2, C_2 < 0$ and $B_1, B_2 = 0$, a γ-type-like INR is produced, where a nodal ring linked two straight nodal lines. Note that we need a find-tuning of B_1 and B_2 parameters to realize the γ-type INR in this two-band model since it generally requires 4 bands.

III. COMPUTATIONAL DETAILS

Our first-principles calculations were based on the density functional theory (DFT) as implemented in the Vienna Ab-initio Simulation Package.[14] The core-valence interactions were described by projector augmented-wave (PAW) potentials within the Perdew-Burke-Ernzerhof (PBE) approximation for the exchange-correlation energy.[15] Plane waves with a kinetic energy cutoff of

500 eV were used as the basis set. We used the conjugate gradient method to optimize the atomic positions, and the energy convergence criterion between two consecutive steps was 10^{-5} eV. The maximum allowed force on the atoms is 10^{-3} eV/Å.

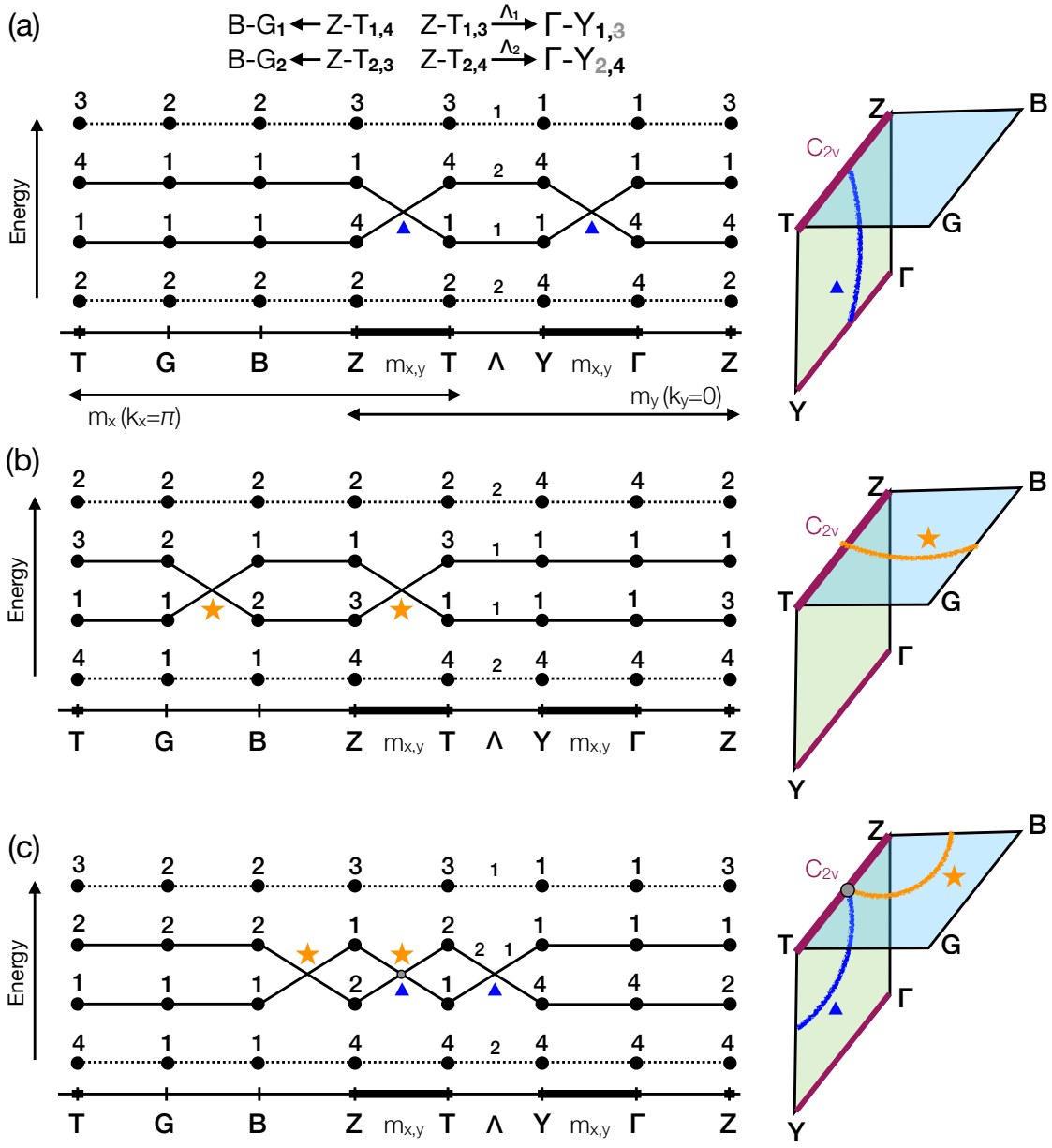

FIG. S3. (color online) Three examples of band structures with two bands contributing to the NLs, where (a) shows the bands induced from 4d (C2) sites near the Fermi level with an open NL on the m_{B} plane as shown in the right panel, while in (b) one band from 4d and another from 4e (Si1) is crossing to form a NL on the m_{B} plane. Note that the NLs can be closed to form nodal rings by inverting bands on the mirror planes. (c) shows the β-type INR, which can be transformed to α-type, or crossing of two open NLs. Note that the nodal intersecting point is marked with grey circle. In the left panels, numbers represent IRREPs at each k-points, and dotted lines depict bands not contributing to the NLs. Band crossings, giving rise to the NLs in the right panels (blue and orange lines), are marked with blue triangles and orange stars.

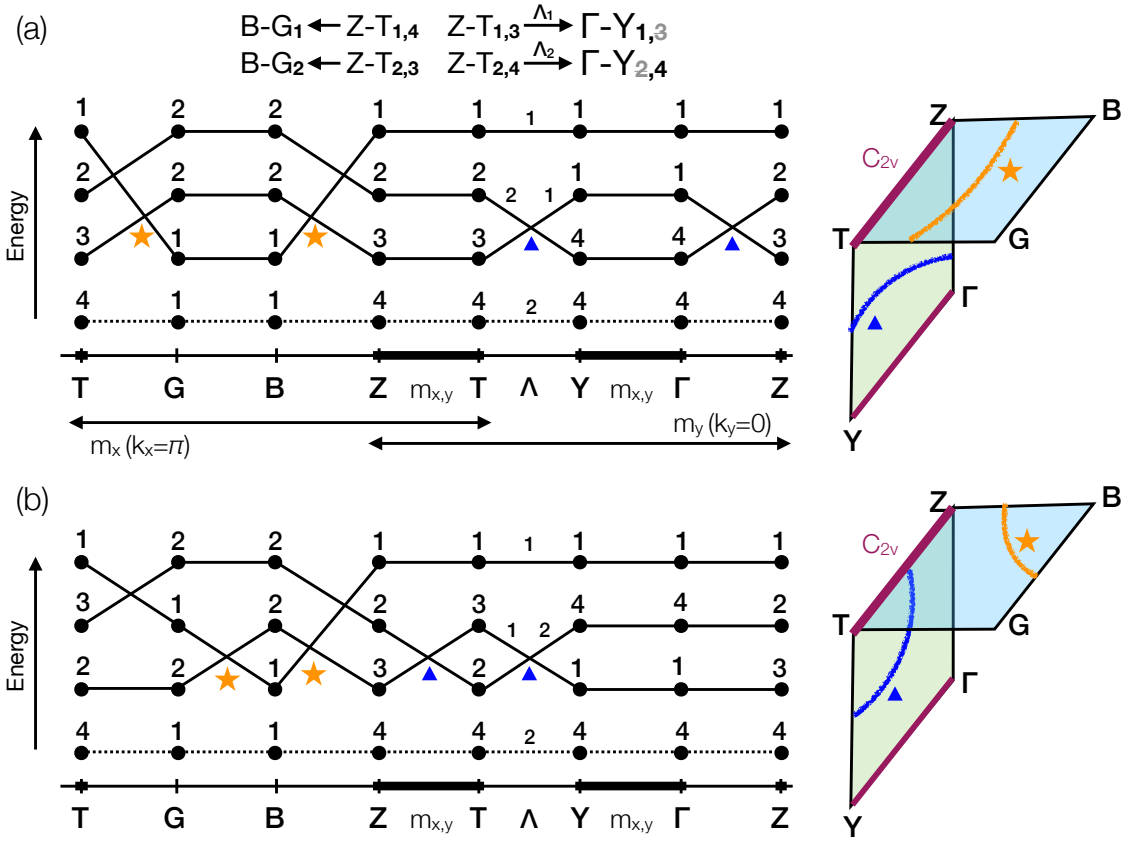

FIG. S4. (color online) Two examples of NLs with three bands, where the two NLs are not sharing the mirror-intersecting Z-T line. (a) Two open NLs, and (b) two nodal rings.

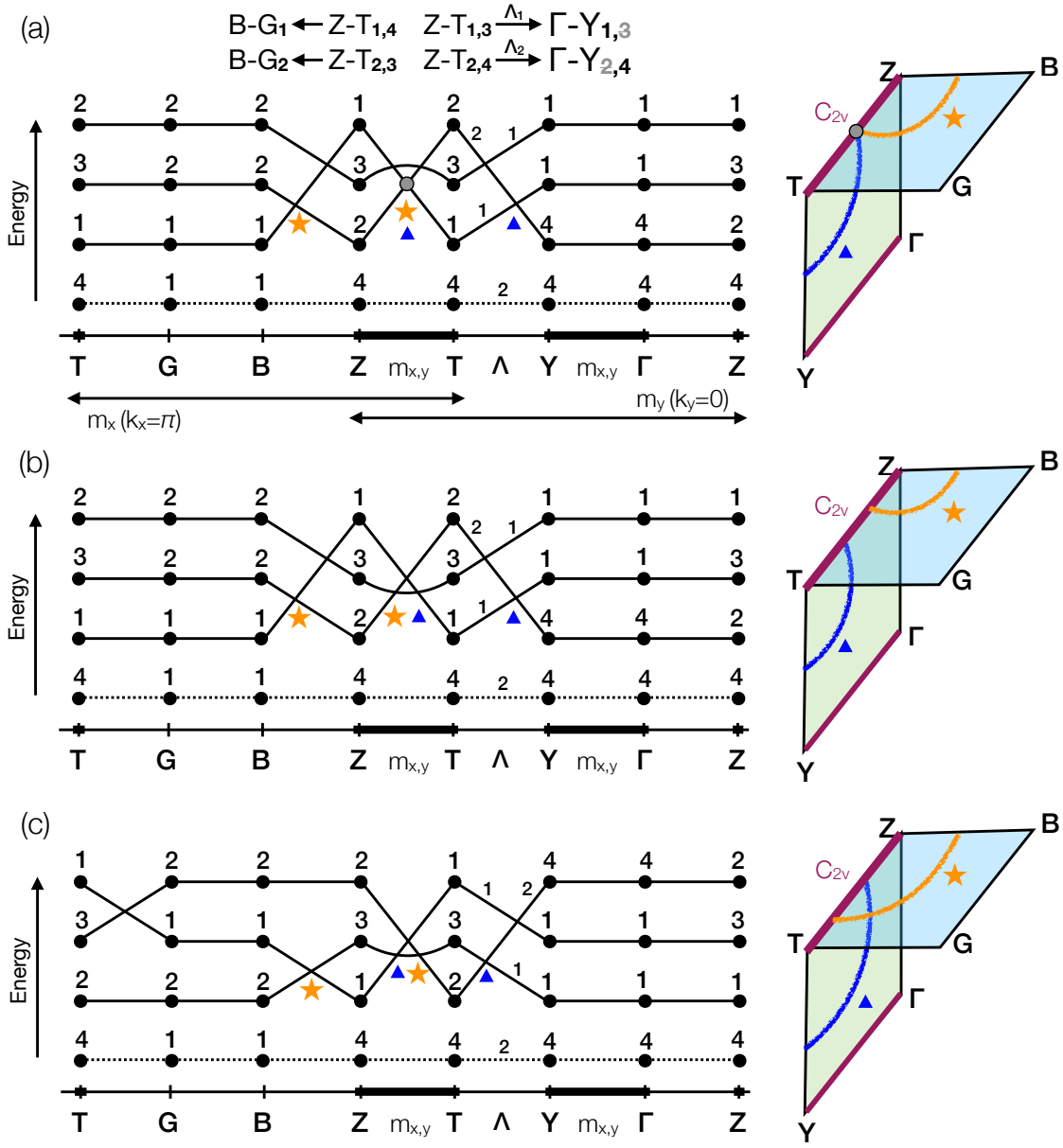

FIG. S5. (color online) Three examples of 3-band-NLs sharing the mirror-intersecting line, where one can have (a) INR, (b) two separate nodal rings, and (c) Hopf link. Note that (a) is actually equivalent to the INR depicted in Fig. S3(c), except the band inversion between $Z_{1,3}$ and $T_{2,3}$ in the unoccupied bands. The nodal intersecting point splits into two separate nodal lines as the $\{Z,T\}_3$ band moves down and is occupied, as shown in (b). (c) shows an example of Hopf link from crossings of three bands. Note that unlike the transition from (a) and (b), transition from (a) (or from (b)) to (c) requires global change of band ordering in the k-space.

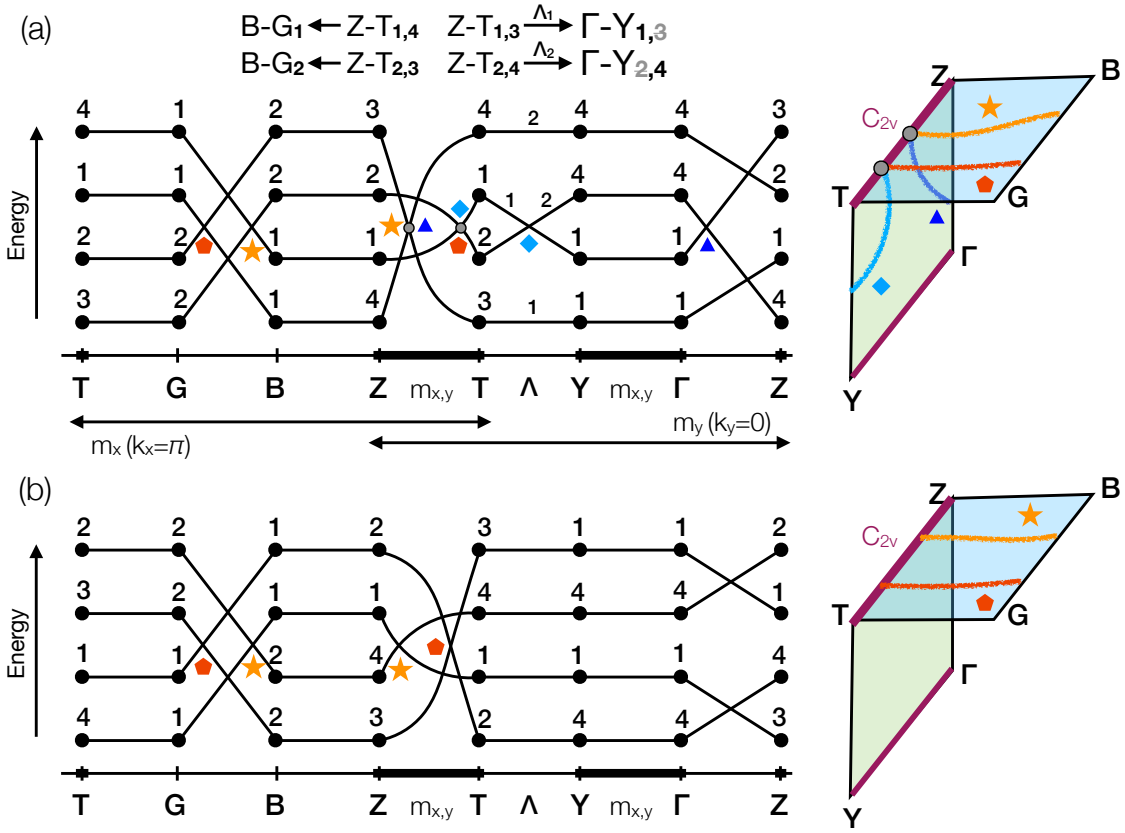

FIG. S6. (color online) Two examples of NLs involving four bands. (a) shows bands with two nodal intersecting points on the Z-T line, which corresponds to the γ-type INR in the manuscript. (b) shows two nodal lines on the $m_{\rm A}$-plane. Note that we can also have two nodal rings on the $m_{\rm A}$-plane by exchanging IRREPs on the Z-T line.

IV. ADDITIONAL SUPPLEMENTARY TABLES AND FIGURES

		θ (Å)	a (Å)	c (Å)	Bond length (Å)	Cohesive energy (eV/atom)
Layered honeycomb structures ($Cmmm$)	BN	64.0	4.424	2.495	1.43-1.70	6.270
	AlP	68.6	6.224	3.926	2.16-2.55	3.303
	GaP	87.9	4.942	3.978	2.10-2.42	2.903
Buckled honeycomb structures ($Amm2$)	SiC	88.9	5.321	3.086	1.77-1.91	6.072
	BP	88.2	5.537	3.193	1.84-1.96	3.606
	BAs	88.1	5.861	3.378	1.95-2.08	2.941

TABLE S1. Structural parameters of the layered and buckled layered structures, consisting of IV or III/V elements. All these structures have topological linked nodal rings.

	θ (deg)	$\epsilon_{1,2}$	$\epsilon_{3,4}$	t_1	t_2	t_3	t_4	t_5	t_6	t_7
BN	64	1.80	-0.90	-1.10	-0.70	-1.50	-0.05	-0.10	0.45	0.10
SiC	89	1.70	-0.90	-1.00	-0.50	-1.20	0.00	0.00	0.45	0.25
	80 (He)	1.70	-0.90	-1.65	-1.00	-1.00	0.15	0.20	0.12	0.10
	108	1.70	-0.90	-0.20	-0.10	-1.40	0.00	0.00	1.10	0.60

TABLE S2. Tight binding parameters (in eV) in Eq. (1) for fitting the DFT band structures in Figs. 4(b-e) in the manuscript.

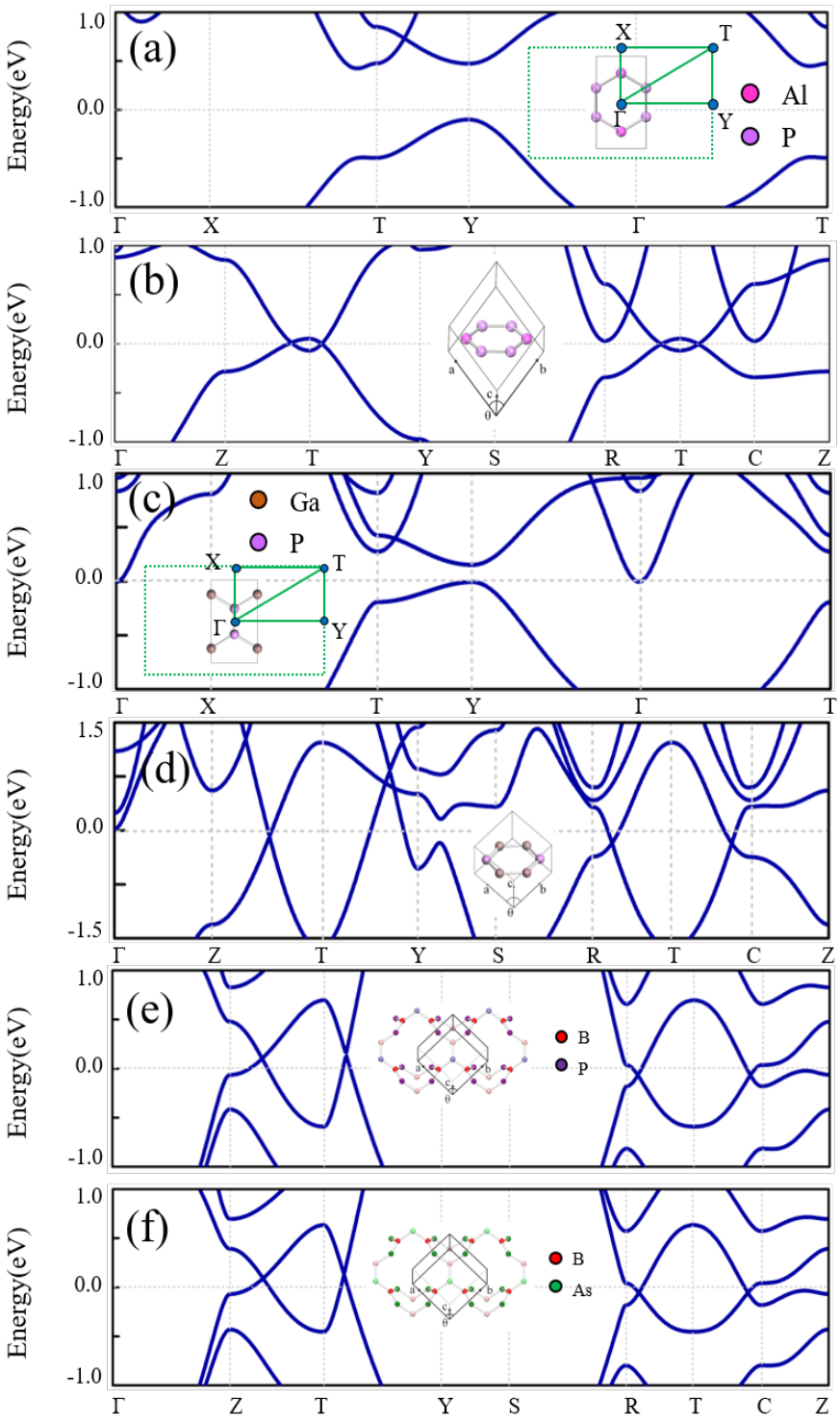

FIG. S7. (color online) Band structures for (a) single-layer AlP, (b) layered 3D AlP, (c) single-layer GaP (d) layered 3D GaP, (e) buckled layered 3D BP and (f) buckled layered 3D BAs.

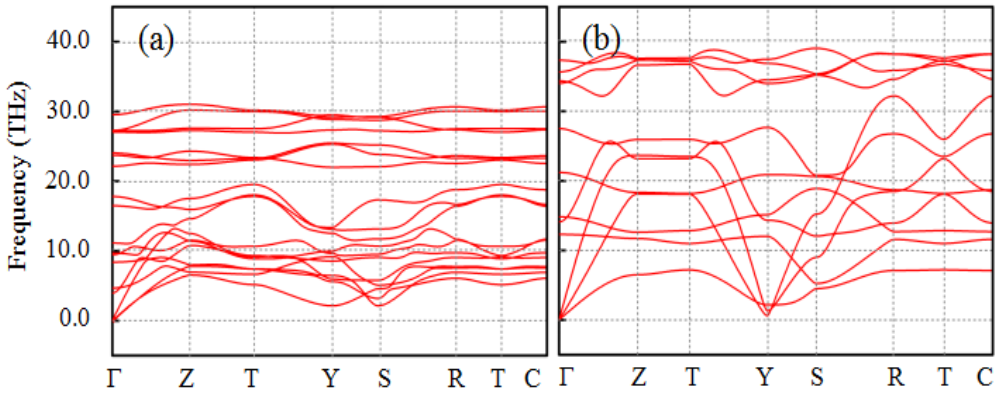

FIG. S8. Phonon dispersions for (a) the buckled layered 3D SiC structure, (b) layered 3D BN structure.

---

[1] B. Bradlyn, L. Elcoro, J. Cano, M. G. Vergniory, Z. Wang, C. Felser, M. I. Aroyo, and B. A. Bernevig, Nature **547**, 298 EP (2017).

[2] M. G. Vergniory, L. Elcoro, Z. Wang, J. Cano, C. Felser, M. I. Aroyo, B. A. Bernevig, and B. Bradlyn, Phys. Rev. E **96**, 023310 (2017).

[3] B. Bradlyn, L. Elcoro, M. G. Vergniory, J. Cano, Z. Wang, C. Felser, M. I. Aroyo, and B. A. Bernevig, arXiv preprint arXiv:1709.01937 (2017).

[4] J. Cano, B. Bradlyn, Z. Wang, L. Elcoro, M. G. Vergniory, C. Felser, M. I. Aroyo, and B. A. Bernevig, arXiv preprint arXiv:1709.01935 (2017).

[5] Note that original studies of BR and their mathematical formulation were done by J. Zak, H. Bacry, and L. Michel for spinless electrons.[9,10] Recent works[1–4] are generalization of the original theory to spinful systems and their utilization in finding topologically nontrivial band structures.

[6] Y. Kim, B. J. Wieder, C. L. Kane, and A. M. Rappe, Phys. Rev. Lett. **115**, 036806 (2015).

[7] *http://www.cryst.ehu.es*.

[8] L. Elcoro, B. Bradlyn, Z. Wang, M. G. Vergniory, J. Cano, C. Felser, B. A. Bernevig, D. Orobengoa, G. de la Flor, and M. I. Aroyo, Journal of Applied Crystallography **50**, 1457 (2017).

[9] J. Zak, Phys. Rev. Lett. **45**, 1025 (1980).

[10] H. Bacry, L. Michel, and J. Zak, Phys. Rev. Lett. **61**, 1005 (1988).

[11] A. Bouhon and A. M. Black-Schaffer, arXiv preprint arXiv:1710.04871 (2017).

[12] Note that TR symmetry plays more important role in constraining the form of Hamiltonian and enforcing degeneracy when we have inversion symmetry, spin degrees of freedom, or rotational symmetry more

then three-fold.

[13] G. Chang, S.-Y. Xu, X. Zhou, S.-M. Huang, B. Singh, B. Wang, I. Belopolski, J. Yin, S. Zhang, A. Bansil, H. Lin, and M. Z. Hasan, Phys. Rev. Lett. **119**, 156401 (2017).

[14] G. Kresse and J. Hafner, Phys. Rev. B **47**, 558 (1993).

[15] J. P. Perdew, K. Burke, and M. Ernzerhof, Phys. Rev. Lett. **77**, 3865 (1996).